On the high-temperature stability of the Al_8Cu_3Ce intermetallic in an additively manufactured Al-Cu-Ce-Zr alloy

F. Theska[1], Y. Yang[2], K.D. Sisco[3], A. Plotkowski[2], S. Primig[1]

[1] School of Materials Science & Engineering, UNSW Sydney, NSW 2052, Australia

[2] Materials Science & Technology Division, Oak Ridge National Laboratory, Oak Ridge, TN 37830, USA

[3] Materials Science and Engineering, University of Tennessee, Knowville, TN 37996, USA

Abstract

High-temperature resistant eutectic Al alloys are crucial materials for lightweight and energy efficient design in the automotive and aviation industries. Among other benefits, additive manufacturing offers a unique pathway to refine eutectic microstructures and develop novel alloys with superior high temperature strength. High-volume fraction intermetallic Al-Cu-Ce alloys have been developed to deliver high temperature strength in combination with reduced hot tearing susceptibility. Zr is added to provide additional strengthening via nanoscale Al_3Zr precipitation, and to stabilize and avoid coarsening of the Al_8Cu_3Ce phase. However, the detailed interaction between Zr and Al_8Cu_3Ce remain unexplored. In this work, we show with synchrotron X-ray diffraction that laser powder bed fusion fabricated Al-Cu-Ce and Al-Cu-Ce-Zr alloys contain predominantly the Al_8Cu_3Ce intermetallic in the as-fabricated condition. Heat treatment of the Al-Cu-Ce alloy results in the $Al_8Cu_3Ce \rightarrow Al_8Cu_4Ce$ phase transformation. In the Al-Cu-Ce-Zr alloy, minor fractions of $(Al,Cu,Si)_4Ce$ and Al_2Cu-θ are also found in the as-fabricated condition, while Al_8Cu_3Ce remains stable during heat treatment. Atom probe microscopy quantifies intermetallic stoichiometries and reveals how Zr is enriched at the Al-matrix / Al_8Cu_3Ce interface acting as a diffusion barrier against solute exchange. Calibrated

thermodynamic modeling underpins this observation as a kinetic effect. A qualitative microstructural model summarizes, how Zr stabilizes Al_8Cu_3Ce against phase transformations and coarsening.

Graphical abstract

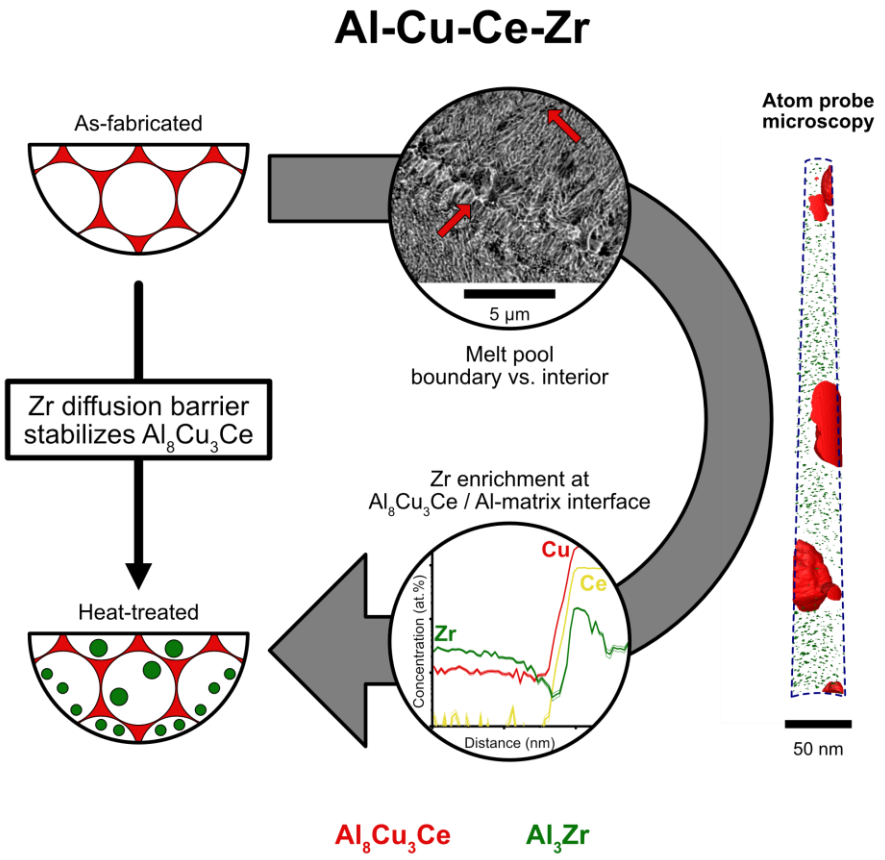

Keywords

Aluminum alloys; Intermetallic phases; Phase transformations; Modeling; Atom probe tomography (APT)

Highlights

- Synchrotron XRD shows $Al_8Cu_3Ce \rightarrow Al_8Cu_4Ce$ transformation in the Al-Cu-Ce alloy
- Atom probe microscopy shows that Zr stabilizes Al_8Cu_3Ce in the Al-Cu-Ce-Zr alloy
- Stoichiometries are quantified for Al_8Cu_3Ce, $(Al,Cu,Si)_4Ce$, Al_2Cu-θ, and Al_3Zr after laser powder bed fusion and heat treatment
- Zr is enriched at the Al-matrix / Al_8Cu_3Ce interface and acts as diffusion barrier
- Nanoscale Al_3Zr precipitates are formed in the Al-matrix in the Al-Cu-Ce-Zr alloy

1. Introduction

The high specific strength of Al alloys makes them attractive materials for light weight mechanical design in the aviation and automotive industries [1–3]. However, a major challenge is to unlock high-temperature mechanical properties for service above 200°C, or ~ 0.5 of the homologous melting temperature [4,5]. Layer-by-layer fabrication of parts via additive manufacturing (AM) is one pathway promising superior properties in comparison to conventionally processed Al alloys [5]. Unique cooling and solidification conditions during AM enable flexibility in the design of components with refined microstructures and improved mechanical properties [6,7]. The high cooling rates during AM unlock novel alloy compositions with potential to increase supersaturation in solid solution and thus, promote increased volume fractions of strengthening phases [8,9]. In a comprehensive review, Michi et al. identified high-temperature precipitation strengthened alloys, high-volume fraction intermetallic alloys and ceramic dispersion alloys as the most promising candidates [5]. Al-Cu-Ce-(Zr) alloys belong to the group of high-volume fraction intermetallic alloys. Dense networks of Ce-rich intermetallic phases provide strengthening at temperatures reaching up to 400°C [10,11], or coarsening resistance up to 500°C [12].

The alloying elements Cu, Ce, Zr and Si have gained interest in recent years. Cu and Si are additions with high solubility in the Al-matrix [4]. Si promotes the formation of a eutectic which

is beneficial for processability through avoiding solidification cracking [13], and Si in solid solution provides additional strengthening, particularly when high cooling rates in AM result in extended solubility [14,15]. Cu promotes the formation of various intermetallic phases, and Al_3Cu-θ'', Al_2Cu-θ', and Al_2Cu-θ are most frequently reported [16,17]. Zr exhibits limited solubility in the Al-matrix, but experimental observations have shown the potential for supersaturation during AM processing, as mentioned above [9]. Thus, strengthening $L1_2$-ordered Al_3Zr precipitates may be formed during heat treatments [18–21]. Ce exhibits near-zero solubility in the Al-matrix and forms various intermetallic phases [22]. Al_4Ce is usually formed as a high-temperature phase, whereas $Al_{11}Ce_3$ or Al_3Ce are reported to form at lower temperatures [7].

Some of the current authors have recently reported the Al_8Cu_3Ce and Al_8Cu_4Ce phases in AM Al-Cu-Ce-(Zr) alloys [8]. It has been shown that Zr additions stabilize Al_8Cu_3Ce against transforming into Al_8Cu_4Ce. Furthermore, the Al_8Cu_3Ce phase also appears more resistant against spheroidization. In previous studies, Shower et al. [16] and Poplawsky et al. [23] found that Zr and Si preferentially segregate to Al-matrix / Al_2Cu-θ' interfaces and reduce Al_2Cu-θ' coarsening kinetics. Fuller et al. demonstrated how Zr forms Al_3Zr shells around Al_3Sc to slow the coarsening rate of nanoscale $Al_3(Zr,Sc)$ precipitates [20,21]. However, the Al_8Cu_3Ce intermetallic has been reported only recently and microstructural heterogeneities depending on local solidification rates and thermal gradients are common in AM parts [24]. Thus, the detailed influences of Zr with respect to melt pool boundaries (MPBs) and melt pool interior (away from MPBs) remain ambiguous and yet to be explored.

Hence, the present work sets out to understand the influence of Zr additions on the stability of the Al_8Cu_3Ce intermetallic in Al-Cu-Ce-(Zr) alloys. Two Al-Cu-Ce and Al-Cu-Ce-Zr alloys are manufactured using laser powder bed fusion (LPBF) and compared in their responses to iso-thermal heat treatments. Synchrotron X-ray diffraction (XRD) is used to distinguish the Al_8Cu_3Ce and Al_8Cu_4Ce intermetallic phases [8]. To isolate the influence of Zr with near-atomic resolution, the Al-Cu-Ce-Zr alloy is then characterized using atom probe

microscopy (APM) [25,26]. Scanning electron microscopy (SEM) micrograph analysis approaches are used to identify MPBs and APM experiments are calibrated to accurately capture the Al-matrix and intermetallic phases. This allows the identification and characterization of the composition of the Al-matrix, various intermetallic phases, and their interfaces, with respect to their location relative at MPBs versus away from MPBs. Al_8Cu_3Ce, $(Al,Cu,Si)_4Ce$, Al_2Cu-θ, and Al_3Zr are quantified in their stoichiometry, and depletion or enrichment zones of Cu and Zr are found at the Al-matrix / Al_8Cu_3Ce interface. Experimental observations are underpinned by thermodynamic modeling and a qualitative microstructural model is derived. This highlights Zr enrichment on the Al-matrix / Al_8Cu_3Ce interface acting as a diffusion barrier which stabilizes this intermetallic against the phase transformation $Al_8Cu_3Ce \rightarrow Al_8Cu_4Ce$.

2. Materials & Methods

2.1. Fabrication & heat treatment

The supplied alloys were cast and atomized by Eck Industries and Connecticut Engineering Associates Corporation, respectively. Cylindrical test samples (115 mm length and 15 mm diameter) were fabricated using a Concept Laser M2 LPBF system. Isothermal heat treatments were carried out as follows: 400°C for 1, 8, 24, 48, and 96 h was used for synchrotron XRD. 350°C for 8 h was used for APM characterization to achieve peak hardness as reported by Bahl et al. [8]. The chemical composition of the as-fabricated samples is provided in Table 1 as measured by inductively coupled plasma spectroscopy. For detailed manufacturing parameters please refer to a companion publication by Bahl et al. [8].

Table 1 Bulk chemical composition of the investigated Al-Cu-Ce and Al-Cu-Ce-Zr alloys [8].

Alloy (at.%)	Al	Cu	Ce	Zr	Si	Fe
Al-Cu-Ce	95.26	3.61	1.00	-	0.07	0.06
Al-Cu-Ce-Zr	94.71	3.73	1.19	0.27	0.05	0.05

2.2. Synchrotron X-ray diffraction

Synchrotron XRD was carried out in the 11-BM facilities of the Advanced Photon Source at Argonne National Laboratory (Lemont, IL, USA). A Debye-Scherrer configuration was used with a wavelength calibrated at 0.458105 nm and a normalization factor of 8.1432. Diffractograms were recorded at ambient temperature between -6.0 and 28.0° 2θ with a step size of 0.001°, 0.1 s dwell time per step and a goniometer radius of 1,000 mm. Diamond files were used to load powder samples in Kapton® tubes. Diffractograms were indexed using structural files as provided in Table 2.

Table 2 Structural data used to index synchrotron XRD data.

Phase	Space group	a (nm)	b (nm)	c (nm)	α (°)	β (°)	γ (°)	Reference
Al-matrix	Fm-3m	0.4050				90		COD9012002 [27,28]
Al_8Cu_3Ce	Pm-3m	0.8510				90		COD1531015 [27,29]
Al_8Cu_4Ce	I4/mmm	0.8500		0.5170		90		SD0458767 [30]

2.3. SEM imaging & melt pool boundary identification

Overview SEM images as shown in Figure 1a and b were acquired using a Hitachi S4800 SEM. SEM imaging of atom probe specimens used a Zeiss Sigma HD field emission SEM with a high-resolution backscattered electron detector (HRBSD). An acceleration voltage of 20 kV, high current mode, and a working distance of ~ 8 mm were chosen. For the MPB identification, FIJI ImageJ was used with a sequence of background subtraction, brightness

and contrast adjustment, and brightness thresholding [31]. Brighter intermetallic structures were then skeletonized and watershed to the tip contour. As shown in Figures 1b, c and d, specimens close to the MPB exhibited larger intermetallic spacing or a more globular intermetallic morphology. Away from the MPB, the morphology was more regular in spacing and less globularly shaped.

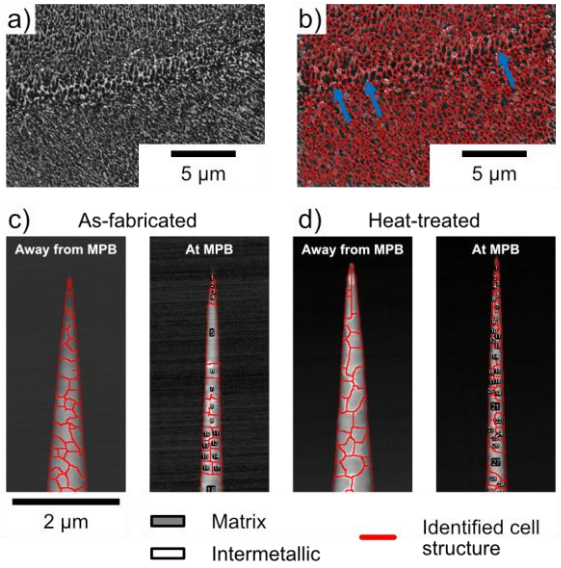

Figure 1 a) Overview SEM micrograph of the Al-matrix and intermetallic. b) Tracing the intermetallic reveals larger cellular spacing at the MPB (see arrows). c) Atom probe specimens in as-fabricated condition away from and at the MPB. d) Atom probe specimens in heat-treated condition away from and at the MPB.

2.4. Atom probe microscopy

APM experiments were carried out for samples in the as-fabricated condition and aged at 350°C for 8 h. APM specimens were prepared using standard techniques [25]. Cuboidal blanks in the dimensions 0.5 x 0.5 x 1.5 mm^3 were cut using a water-cooled Struers Minitom diamond blade. Two stage electropolishing used 20 % and 5 % perchloric acid solutions at ambient temperature and voltages ranging from 20 to 10 V. Immediately after final electropolishing, batches of 3-4 specimens were transferred into a Zeiss Sigma HD FEG SEM

to avoid oxidation. SEM-BSE imaging allowed screening for specimens away from or at MPBs. Undesired specimens were again electropolished, specimens of interest were then immediately transferred into a Cameca LEAP 4000X Si to minimize oxidation. Atom probe data acquisition parameters were 35K temperature, 200 kHz pulse frequency, 1.0 % detection rate, and a laser energy of 30 pJ. The laser energy was calibrated with small datasets containing 1 and 5 million atoms. This is required to compromise between homogeneous evaporation, mass resolving power at the full width half maximum (FWHM), and the Ce^{+3} / Ce^{+2} ratio as provided in supplementary Figure S1. The laser energy of 30 pJ was favorable to meet these criteria and an exemplary mass spectrum is provided in supplementary Figure S2. The major peak overlap between $^{94}Zr^{+2}$ and $^{140}Ce^{+3}$ between 40 to 50 Da is minimized as most $^{140}Ce^{+2}$ evaporates at ~ 70 Da. H, Mg, Ti, AlO, AlOH are attributed as artefacts and thus ignored in subsequent analyses. Despite Table 1 providing Fe in small amounts in all alloys, no Fe could be identified in the mass spectrum as they may be obscured by the thermal tail of $^{27}Al^{+1}$. All subsequent reconstructions and data analyses were carried out in the Cameca AP Suite 6. In the as-fabricated condition, compositions of Al-matrix and Al_8Cu_3Ce were extracted from volumes separated by iso-concentration surfaces of 20 at.% Cu+Ce. In the heat-treated condition, Al-matrix and Al_3Zr were separated by additional iso-concentration surfaces of 5 at.% Zr. Compositional profiles across the Al-matrix / Al_8Cu_3Ce interface were extracted using proximity histograms for individual intermetallic particles in a step size of 0.5 nm and width of 20 nm. For all provided measurements, peak decomposition and background corrections were carried out.

2.5. Thermodynamic calculation

Two types of thermodynamic calculations were performed, where the first one is to calculate the solidification path following the Scheil model [32] to assess the phases formed during the AM solidification process. The second one is to calculate phases following the lever-rule model to assess phases formed during isothermal heat treatments. Computer coupling of phase

diagrams and thermo-chemistry, i.e., the CALPHAD approach [33] was used to develop a thermodynamic database of Al-Cu-Ce-Zr required to perform these calculations. The Gibbs energy functions of the four unary systems Al, Ce, Cu, and Zr were adopted from the SGTE (Scientific Group Thermodata Europe) [34]. The Gibbs energy functions of phases in Al-Cu, Al-Ce, Cu-Ce, and Al-Cu-Ce were modified from Bo et al. [35]. Those for phases in Al-Cu, Al-Zr, and Al-Cu-Zr were modified from Zhou et al. [36]. The Gibbs energy functions of the Al-Ce-Zr and Ce-Cu-Zr systems were obtained from extrapolation of constituent binary systems. The detailed modeling process and the comparison between calculated and experimental data will be presented elsewhere. This work will primarily present results focusing on the calculated solidification path based on the Scheil model and equilibrium calculation based on the lever-rule model.

3. Results

3.1 Zr additions stabilize Al_8Cu_3Ce

Synchrotron XRD diffractograms are summarized in Figure 2. Figure 2a shows the Al-Cu-Ce alloy, without Zr additions. Peaks in the as-fabricated condition correspond to the Al-matrix and Al_8Cu_3Ce high-temperature intermetallic. After heat treatment at 400°C for 1 h, peaks around 8.4° and 11.8° 2θ develop as highlighted by black arrows. This corresponds to the phase transformation $Al_8Cu_3Ce \rightarrow Al_8Cu_4Ce$. The diffractogram for prolonged heat treatment for up to 96 h at 400°C exhibits peak sharpening but no additional peaks.

Figure 2b shows diffractograms for the Al-Cu-Ce-Zr alloy. In the as-fabricated condition, the peaks appear similar to the Al-Cu-Ce alloy, where only the Al-matrix and Al_8Cu_3Ce intermetallic are identified. Prolonged heat treatment at 400°C for 1 to 96 h exhibits no indications of a transformation of the Al_8Cu_3Ce intermetallic. The increase in peak intensity and sharpness may be indicative of coarsening, residual stress relief, or chemical homogenization [37]. Thus, the high-temperature intermetallic Al_8Cu_3Ce is stabilized by Zr

additions, as highlighted by black arrows. Peaks for other phases, such as Al_3Zr, Al_4Ce or $Al_{11}Ce$ provide no match or overlap with existing peaks, and therefore remain ambiguous. Hence, the following sections focus on APM characterization of the Al-Cu-Ce-Zr alloy and omit the Zr-free Al-Cu-Ce alloy. This is an attempt to isolate the stabilizing effect of Zr on the Al_8Cu_3Ce phase.

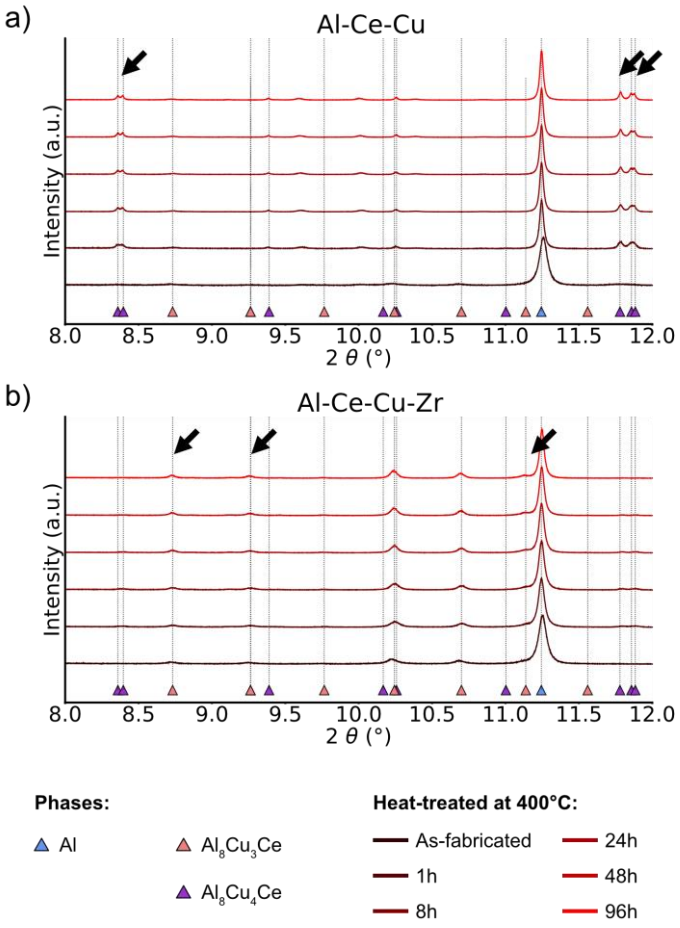

Figure 2 Indexed synchrotron XRD diffractograms. a) The Al-Cu-Ce alloy shows some Al_8Cu_3Ce in the as-fabricated condition and Al_8Cu_4Ce (see arrows) is formed during heat treatment. b) The Al-Cu-Ce-Zr alloys shows Al_8Cu_3Ce (see arrows) in the as-fabricated and heat-treated conditions.

3.2. Qualitative compositions of Al-matrix & intermetallic phases

Figure 3 shows APM data acquired in the as-fabricated condition, away from the MPB. In the corresponding SEM image, the Al-matrix and intermetallic can be recognized as dark and

bright regions, respectively. APM atom maps are provided in side-view and the Al map in blue shows that the intermetallic phase displaces the Al-matrix. Cu and Ce maps in red and yellow highlight the presence of two types of intermetallic phases: (I) Cu-rich and (II) Cu-Ce-rich. Additional Cu segregation is found, likely decorating a line defect. The Zr map in green shows the supersaturation of the Al-matrix and subtle enrichments in (II). However, no Al_3Zr precipitates are found in this condition. The Si map in grey shows some presence in the Al-matrix as well as (II). Finally, intermetallic phases are enveloped by 20 at.% Cu+Ce iso-concentration surfaces. The location of the large Cu-Ce-rich intermetallic correlates well with the location observed in the SEM image. Complementary representations of the data acquired from the as-fabricated condition at the MPB, heat-treated away from the MPB and heat-treated at the MPB are provided in the following Figure 4,Figure 5, andFigure 6, respectively.

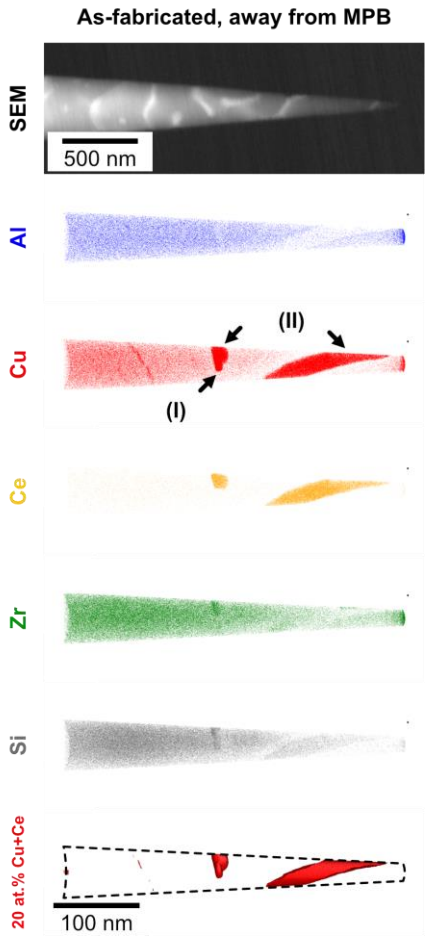

Figure 3 SEM image of an atom probe specimen in as-fabricated condition away from the MPB. Individual atom maps present the data from the same condition and location in side-view for Al, Cu, Ce, Zr, and Si. 20 at.% Cu+Ce iso-concentration surfaces are used to distinguish between the Al-matrix and intermetallic phases.

In the as-fabricated condition, away from the MPB (see Figure 4), Al is displaced by intermetallic phases. Cu and Ce maps indicate the presence of Cu-rich (I) and Cu-Ce-rich (II) intermetallic phases. The Zr map indicates the supersaturation of the Al-matrix and some subtle enrichment in (II). No indications of Al_3Zr can be found in the Al-matrix. The Si map reveals an additional Cu-Ce-Si-rich intermetallic (III), that is not observed in the data away from the MPB. The observed intermetallic phases are enveloped by a 20 at.% Cu+Ce iso-concentration surface and correlate well with the locations observed in the SEM image.

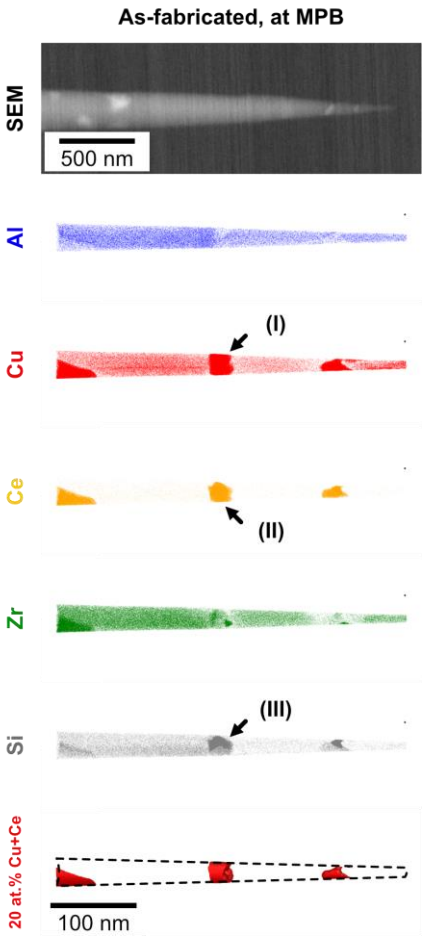

Figure 4 SEM image of an atom probe specimen in as-fabricated condition at the MPB. Individual atom maps present the data from the same condition and location in side-view for Al, Cu, Ce, Zr, and Si. 20 at.% Cu+Ce iso-concentration surfaces are used to distinguish between the Al-matrix and intermetallic phases.

The heat-treated condition, away from the MPB is shown in Figure 5. Al is displaced by the Cu-Ce rich intermetallic (IV). Here the Zr map shows significant enrichment in (IV), whereas the Al-matrix exhibits a Zr depletion zone around (IV). Within the Al-matrix, nanoscale Al_3Zr precipitates (V) are found as localized enrichments in Zr. Si segregates into (IV) instead of the Al-matrix. The intermetallic (IV) is enveloped by 20 at.% Cu+Ce iso-concentration surfaces and (V) is enveloped by 5 at.% Zr iso-concentration surfaces. Thus, a depletion zone of (V) around (IV) becomes evident.

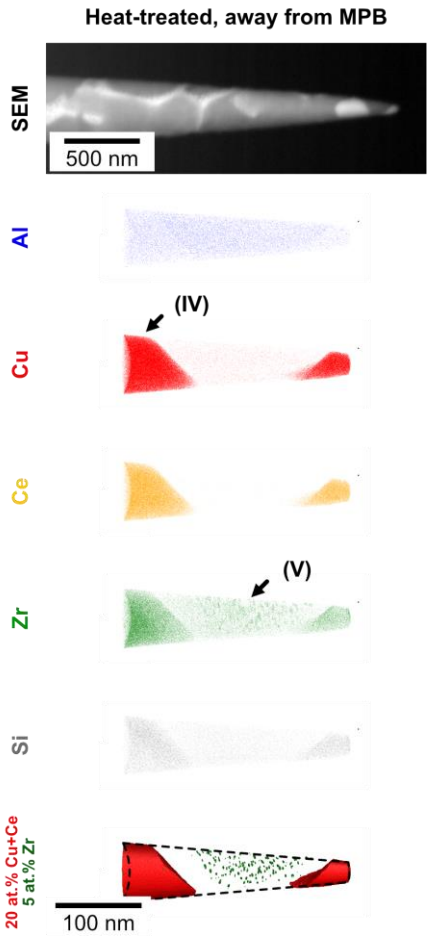

Figure 5 SEM image of an atom probe specimen in heat-treated condition away from the MPB. Individual atom maps present the data from the same condition and location in side-view for Al, Cu, Ce, Zr, and Si. 20 at.% Cu+Ce iso-concentration surfaces are used to distinguish between the Al-matrix and intermetallic phases. 5 at.% Zr iso-concentration surfaces reveal the presence of Al_3Zr precipitates.

Finally, the heat-treated condition, at the MPB is presented in Figure 6 where the Al-matrix and Cu-Ce-rich intermetallic (IV) exhibit similar features as observed in Figure 5. Localized enrichments in Zr indicate the presence of nanoscale Al_3Zr precipitates (V) within the Al-matrix. Zr and Si are also substantially enriched in (IV). 20 at.% Cu+Ce iso-concentration surfaces envelop (IV), while 5 at.% Zr iso-concentration surfaces envelop (V). More subtle than in Figure 5, depletion zones of (V) around (IV) become evident. Based on their chemical compositions, one can identify the intermetallic phases in Figure 3,Figure 4,Figure 5,

andFigure 6 as follows: (I) is Al_2Cu-θ; (II) & (IV) are Al_8Cu_3Ce, (III) is a Si-rich Al_4Ce-type $(Al,Cu,Si)_4Ce$, and (V) is identified as Al_3Zr.

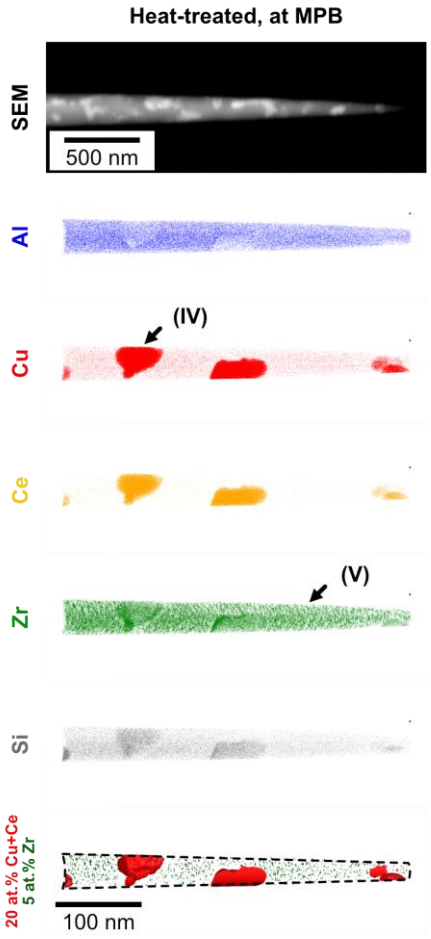

Figure 6 SEM image of an atom probe specimen in heat-treated condition at the MPB. Individual atom maps present the data from the same condition and location in side-view for Al, Cu, Ce, Zr, and Si. 20 at.% Cu+Ce iso-concentration surfaces are used to distinguish between the Al-matrix and intermetallic phases. 5 at.% Zr iso-concentration surfaces reveal the presence of Al_3Zr precipitates.

3.3. Quantitative composition of Al-matrix, intermetallic phases & interfaces

Table 3 summarizes the composition of the Al-matrix depending on the condition and location with respect to MPBs. Independent of MPB location and condition, detected Ce levels are negligible. In the as-fabricated condition, Cu levels of ~ 0.5 at.% are found away from the MPB and at the MPB. In the heat-treated condition, this is significantly reduced to ~ 0.03 at.% Cu

in both locations. In the as-fabricated condition, Zr is more highly supersaturated in the Al-matrix away from the MPB than at the MPB. However, in the heat-treated condition, this is reduced to ~ 0.02 at.% Zr in both locations. This trend is inverted for Si, where 0.05 and 0.03 at.% are found at the MPB and away from the MPB, respectively. Only negligible amounts of Si are found in the heat-treated condition.

Table 3 Al-matrix compositions as obtained from APM in at.%. Displayed are average values and standard deviations in parentheses.

Condition	Location	Al	Cu	Ce	Zr	Si
As-fabricated	**Away from MPB**	99.26 (0.01)	0.47 (0.01)	< 0.01	0.24 (0.01)	0.03 (0.01)
	At MPB	99.26 (0.01)	0.47 (0.01)	< 0.01	0.21 (0.01)	0.05 (0.01)
Heat-treated	**Away from MPB**	99.96 (0.01)	0.02 (0.01)	< 0.01	0.02 (0.01)	< 0.01
	At MPB	99.95 (0.01)	0.03 (0.01)	< 0.01	0.02 (0.01)	< 0.01

Table 4 provides compositions of the intermetallic phases identified in the previous section. In the as-fabricated condition, away from the MPB, Al_2Cu-θ (I), Al_8Cu_3Ce (II), and Al_3Cu-θ'' (at line defect) are found. Al_2Cu-θ is stoichiometric, but Al_8Cu_3Ce is enriched in Al. Al_3Cu-θ'' also appears enriched in Al, however, this is likely an artefact contributed by the surrounding Al-matrix. No Ce is dissolved in Al_2Cu-θ and 0.1 to 0.2 at.% Zr is dissolved in Al_8Cu_3Ce and Al_3Cu-θ''. In the as-fabricated condition, at the MPB, Al_2Cu-θ (I), Al_8Cu_3Ce (II), and $(Al,Cu,Si)_4Ce$ (III) are found. Again, Al_2Cu-θ is stoichiometric, and Al_8Cu_3Ce is enriched in Al. However, here, Al_8Cu_3Ce contains ~ 0.8 at.% more Cu than away from the MPB. $(Al,Cu,Si)_4Ce$ is consistent with the stoichiometry of either Al_4Ce or $Al_{11}Ce_3$, where Al, Cu, and Si share the Al sites (~ 79 at.%) and Ce remains on the Ce sites (~ 21 at.%). However, the quantity is too low to reliably detect the crystallographic structure, but as suggested by Figure 8, this phase

is assigned as Al_4Ce-type. In the heat-treated condition, away from the MPB, Al_8Cu_3Ce (IV), and Al_3Zr (V) are found. Al_8Cu_3Ce appears enriched by ~ 1.6 at.% Cu and is now closer to its ideal stoichiometry. The Zr content is also significantly increased to 1.2 at.%, although this value is accompanied by a large standard deviation of 0.6 at.% Zr. Ce is also somewhat increased while the Si content remains unchanged. Al_3Zr is close to its ideal stoichiometry. Small amounts of Cu, Ce and Si may be found, but the accompanying high standard deviations suggest that this is likely an artefact.

In the heat-treated condition, at the MPB, the same phases (IV) and (V) are found. Al_8Cu_3Ce contains ~ 1.3 at.% more Cu than in the as-fabricated condition and is therefore closer to its ideal stoichiometry. In comparison to the as-fabricated condition, the Zr content is increased, but remains lower than in the heat-treated condition away from the MPB. Al_3Zr is close to its ideal stoichiometry but contains significantly more Zr than away from the MPB. Less Cu, Ce, and Si are recorded which are accompanied by relatively large standard deviations suggesting their presence is an artefact.

Table 4 Compositions of the intermetallic phases for all conditions and locations, as well as identified phase type. Displayed are average values and standard deviations in parentheses.

Condition	Location	Al	Cu	Ce	Zr	Si	Residual.	Type
As-fabricated	Away from MPB	71.1 (2.4)	19.5 (1.6)	8.5 (0.7)	0.2 (0.1)	0.4 (0.1)	< 0.1	Al_8Cu_3Ce
		67.8 (1.2)	32.1 (1.2)	< 0.1	< 0.1	< 0.1	< 0.2	Al_2Cu-θ
		79.1 (5.1)	19.7 (3.1)	0.1 (0.3)	0.3 (0.6)	0.5 (1.2)	< 0.4	Al_3Cu-θ"
	At MPB	71.1 (1.5)	20.7 (1.2)	7.8 (0.7)	0.1 (0.2)	0.2 (0.3)	< 0.1	Al_8Cu_3Ce
		69.3 (1.3)	30.6 (1.4)	< 0.1	< 0.1	< 0.1	< 0.1	Al_2Cu-θ
		49.9 (1.9)	16.5 (1.9)	21.4 (1.8)	0.2 (0.3)	11.9 (1.2)	< 0.1	$(Al,Cu,Si)_4Ce$
Heat-treated	Away from MPB	67.1 (1.1)	21.1 (0.4)	9.5 (0.3)	1.2 (0.6)	0.5 (0.1)	< 0.4	Al_8Cu_3Ce
		72.8 (1.8)	3.4 (0.9)	2.0 (1.0)	20.9 (1.8)	0.9 (0.3)	< 0.1	Al_3Zr
	At MPB	67.9 (0.8)	22.0 (0.5)	9.2 (0.3)	0.2 (0.1)	0.4 (0.1)	< 0.3	Al_8Cu_3Ce
		69.0 (2.7)	1.5 (1.2)	1.2 (0.4)	27.9 (2.4)	0.3 (0.3)	< 0.1	Al_3Zr

Proximity histograms of the Al_8Cu_3Ce intermetallic (labelled as (II) in Figure 3 andFigure 4, and (IV) in Figure 5 andFigure 6) are provided in Figure 7. In the as-fabricated condition, away from the MPB, a Cu depletion zone is found. However, no enrichment or depletion in Zr can be found. Similarly, at the MPB, a Cu depletion zone is present in the as-fabricated condition. In the heat-treated condition, away from and at the MPB, Cu depletion zones are absent. Instead, Zr depletion zones are found in the Al-matrix surrounding Al_8Cu_3Ce, and Zr enrichment zones are found towards the inside of the Al-matrix / Al_8Cu_3Ce interface.

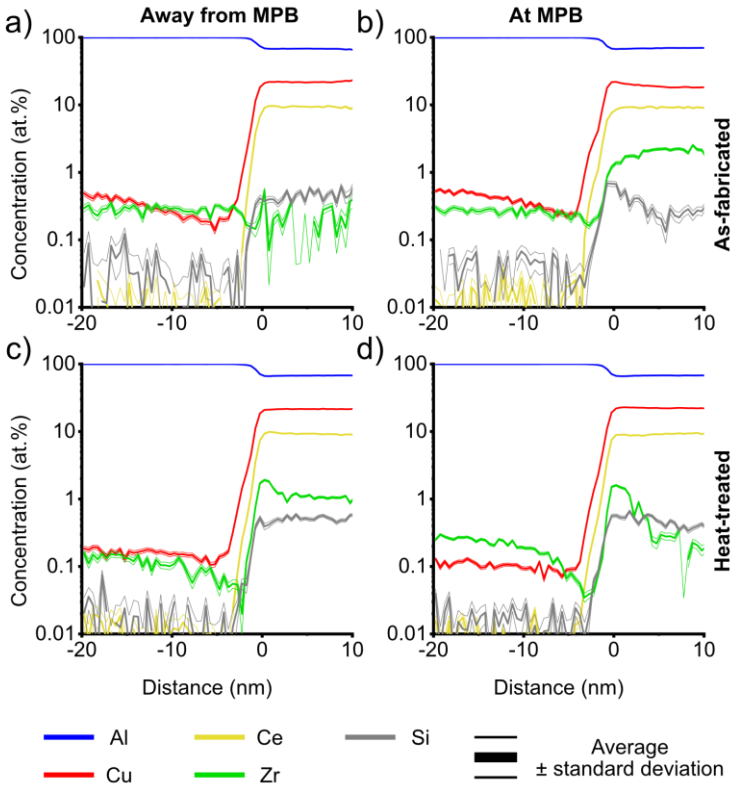

Figure 7 Proximity histograms around Al_8Cu_3Ce. a) as-fabricated, away from MPB, b) as-fabricated, at MPB, c) heat-treated, away from MPB, and d) heat-treated, at MPB.

4. Discussion

4.1. Thermodynamic stability of intermetallic phases

The solidification path following the Scheil model is provided in Figure 8a. Above 620°C, Al-matrix, Al_3Zr and Al_4Ce are formed from the liquid. This is in agreement with previous studies, where cuboidal, primary Al_3Zr precipitates are found along MPBs [5,9,38]. These cuboidal primary Al_3Zr precipitates form directly from the liquid and are often several 100's of nanometers large but also difficult to observe via APM. Primary Al_3Zr capturing Zr from the Al-matrix is likely the cause for the lower Zr matrix composition in the as-fabricated condition, at the MPB (see Table 3). Al_4Ce has been reported as a high-temperature stable intermetallic phase in the Al-Ce system and therefore forms early during solidification [7,39]. Thus, the observed $(Al,Cu,Si)_4Ce$ is assigned as Al_4Ce instead of $Al_{11}Ce_3$. Observations in Figure 4 and Table 4 show that Cu and Si substitute for Al, so that it may be described as $(Al,Cu,Si)_4Ce$. While this has been observed only at the MPB, its presence away from the MPB cannot be excluded due to the limited volumes acquired by APM [25,26]. The intermetallic Al_8Cu_3Ce appears stable over a wide solidification range between 620 and 550°C. However, this intermetallic has been observed only recently, where some of the current authors reported Al_8Cu_3Ce in the Al-Cu-Ce-(Zr) alloy system [8]. Around 550°C, Al_8Cu_4Ce and $Al_{68}Cu_{15}Zr_{17}$ are expected to form in negligible amounts within narrower temperature ranges. Below 550°C and 500°C low mole fractions of Al_2Cu-θ and Si, respectively, are expected. Al_2Cu-θ has been observed in the as-fabricated condition to precipitate directly onto Al_8Cu_3Ce. Al_3Cu-θ" nucleates along line defects, such as dislocations (see Figure 3). However, as only 0.05 at.% Si have been found in Table 1, the $(Al,Cu,Si)_4Ce$ intermetallic captures Si at increased temperatures and suppresses the formation of Si during AM. Thus, Al_8Cu_3Ce, $(Al,Cu,Si)_4Ce$ (Al_4Ce-type), and Al_2Cu-θ are expected in high mole fractions, as shown in Figure 8b.

Figure 8c provides the expected equilibrium mole fractions to assess phase transformations during the heat treatment. Above 620°C, this alloy is expected to melt, whereas Al_3Zr and Al_4Ce are expected to form between 620 and 600°C. Below 600°C, Al_8Cu_3Ce is formed

besides the Al-matrix and Al_4Ce. Around 530°C, the phase transformation $Al_8Cu_3Ce \rightarrow Al_8Cu_4Ce$ is expected, which may be accompanied by the formation of secondary, nanoscale Al_3Zr precipitates. Synchrotron XRD in Figure 2 shows that this phase transformation is inhibited by Zr additions and only takes place in the Al-Cu-Ce alloy. Finally, below 350°C, Si and $Al_{68}Cu_{15}Zr_{17}$ are expected with negligible mole fractions. Figure 8d provides an enlarged region of Figure 8c to allow closer observation of low mole fraction phases.

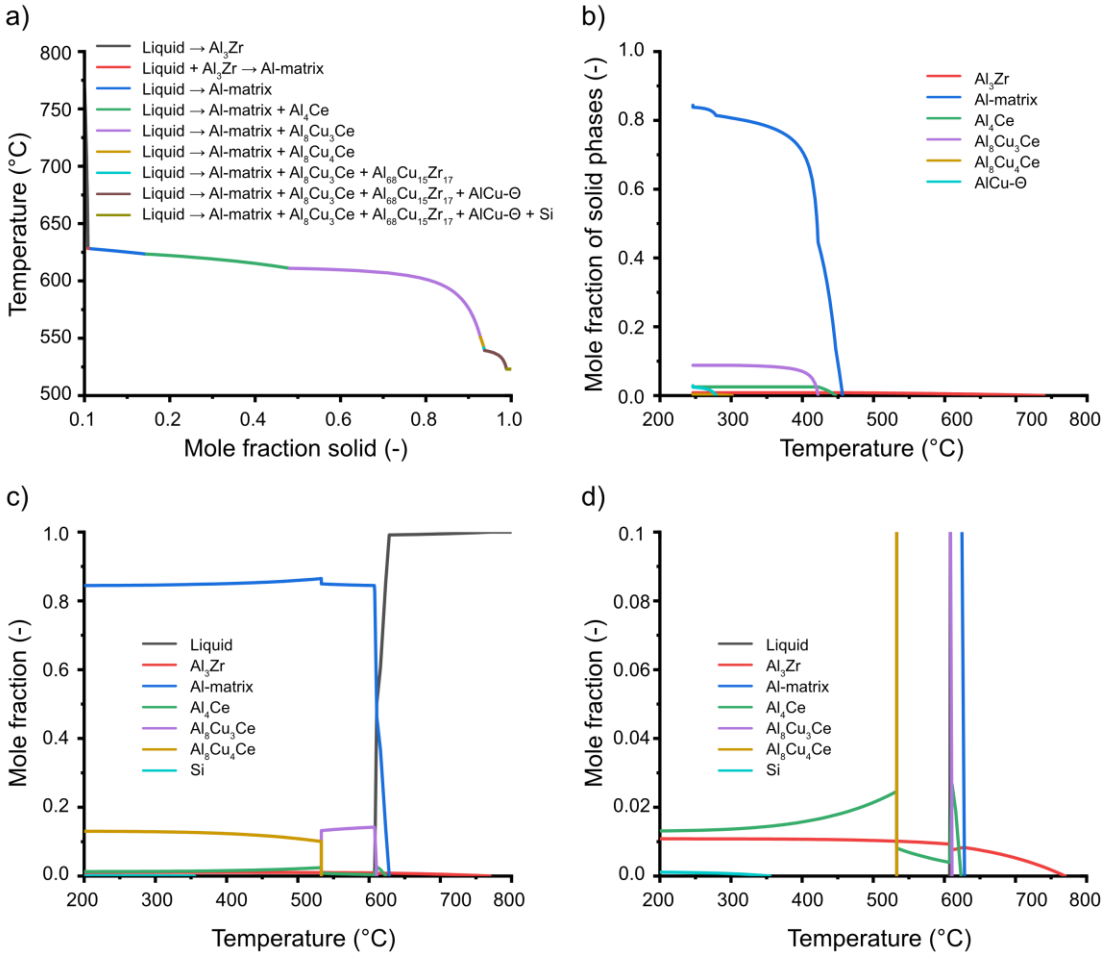

Figure 8 Thermodynamic modeling. a) Solidification path following the Scheil model. Al_4Ce and Al_8Cu_3Ce are formed as high-temperature intermetallic phases. Al_8Cu_4Ce and AlCu-θ are formed at lower temperatures. b) Predicted mole fractions for the solidification path. c) Expected equilibrium mole fractions show that the transformation $Al_8Cu_3Ce \rightarrow Al_8Cu_4Ce$ is expected around ~ 540°C. d) Enlarged region of the expected equilibrium mole fractions to visualize changes in minor phases.

4.2. The role of Zr additions stabilizing Al_8Cu_3Ce

Synchrotron XRD and thermodynamic modeling highlight the role of Zr inhibiting the $Al_8Cu_3Ce \rightarrow Al_8Cu_4Ce$ transformation. However, compositional information of the Al-matrix, Al_8Cu_3Ce, and their interface in Figure 7 provides the insights required to understand this mechanism at the near-atomic scale. Cu depletion zones around Al_8Cu_3Ce are observed in the as-fabricated condition, while Zr depletion zones are found in the heat-treated condition. Figure 9 represents the quantified results of depletion zone width and difference from bulk. In the as-fabricated condition, Cu is depleted up to 20 nm into the Al-matrix by -0.5 at.%. In the heat-treated condition, Zr is depleted up to 10 nm into the Al-matrix by -0.3 at.%. Using the Arrhenius-type equation $D=D_0 \exp\left(-\frac{E_A}{R\,T}\right)$, the diffusivity of Zr in Al at T = 350°C is estimated to $D \sim 3.8 \times 10^{-22}$ m^2 s^{-1} with the pre-exponential $D_0 = 7.28 \times 10^{-2}$ m^2 s^{-1}, activation energy $E_A = 242$ kJ mol^{-1} and $R = 8.314$ J mol^{-1} K^{-1} [40]. For an 8 h heat treatment, the diffusion length may be estimated via $2\sqrt{D\,t}$ [41] as ~ 7 nm. This is in reasonable agreement with Figure 9. Using the same approach, the diffusivity of Cu in Al is estimated to $D \sim 2.6 \times 10^{-16}$ m^2 s^{-1} with $D_0 = 6.54 \times 10^{-5}$ m^2 s^{-1} and $E_A = 136$ kJ mol^{-1} [40]. For an 8 h heat treatment, the diffusion length may be estimated as ~ 5.5 µm. This is in reasonable agreement as no Cu depletion zones are observed after the heat treatment. However, the enrichment of Zr towards the Al-matrix / Al_8Cu_3Ce interface in Figure 7 requires special consideration. Here, the Al-matrix side of the interface is depleted in Zr, whereas the Al_8Cu_3Ce side of the interface is enriched in Zr. Remarkably, no significant differences between the location away from the MPB and at the MPB is observed here.

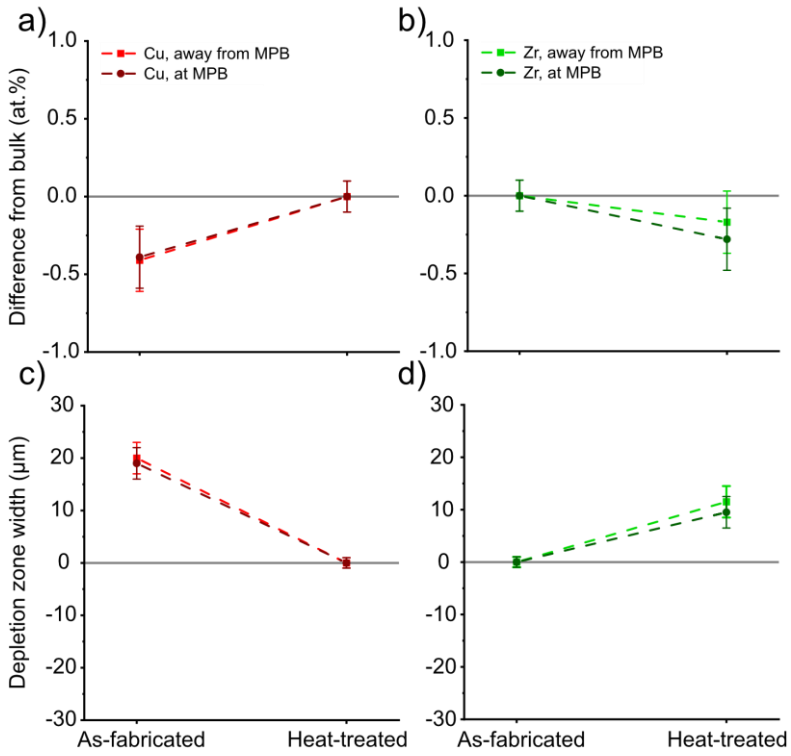

Figure 9 Evolution of the Cu and Zr depletion zones around Al_8Cu_3Ce. a) Cu difference from bulk, b) Zr difference from bulk, c) Cu depletion zone width, and d) Zr depletion zone width. In the heat-treated condition, Zr is also enriched within the intermetallic.

While Ce promotes the formation of Al_8Cu_3Ce, Cu is depleted from the Al-matrix as well (see Figure 8). Thus, the Cu depletion zones observed in the as-fabricated condition must be the result of rapid solidification during AM [42]. This has been suggested in previous work and is confirmed by the low Cu concentration in the Al-matrix after the heat treatment (see Table 3) [39,43]. Table 4 shows that this is the result of Al_8Cu_3Ce enriching by ~ 0.3 to 1.6 at.% Cu during heat treatment at the MPB and away from the MPB, respectively. The depletion of Cu from the Al-matrix is further amplified by the precipitation of Al_2Cu-θ as observed in Figure 3 and Figure 4, and in some of the current authors' previous work [8]. Differences in Zr dissolved in Al_8Cu_3Ce, as shown in Figure 7, are likely the result of different thermal gradients at the MPB and away from the MPB. Depending on thermal gradients and solidification velocities, eutectic solidification or solid-state phase transformations due to solid solution supersaturation

dominate [5,24]. Local differences in solidification velocities between positions at the MPB and away from the MPB may result in the local selection of dendritic Al-matrix solidification or eutectic Al-matrix + Al_8Cu_3Ce solidification. While it is difficult to assess the localized influence of solidification velocities, differences in the partitioning of Zr into Al_8Cu_3Ce may be a function of these local thermal conditions. In the heat-treated condition, away from the MPB, Al_8Cu_3Ce enriches in Zr subsequently and develops the Zr depletion and enrichment zones. However, in the heat-treated condition, at the MPB, Al_8Cu_3Ce has experienced the most time to enrich the Al-matrix / Al_8Cu_3Ce interface with Zr, so that the enrichment and depletion profiles are the most pronounced.

Two competing processes must be considered during the formation of the Zr depletion zone: (i) the formation of nanoscale Al_3Zr captures Zr from the Al-matrix (see Table 3), and (ii) Zr exhibits an affinity towards the Al-matrix / Al_8Cu_3Ce interface, where it is enriched in the intermetallic during heat treatment. Here, Zr behaves similar to previous observations of the Al-matrix / Al_2Cu-θ' interfaces. Shower et al. [16] showed that interfacial energy reduction and solute drag attract Zr to Al-matrix / Al_2Cu-θ' interfaces. Poplawsky et al. [23] observed a synergistic effect of Mn and Zr segregations at Al-matrix / Al_2Cu-θ' interfaces stabilizing Al_2Cu-θ' against coarsening. In the present work, no precipitation of Al_3Zr on the Al-matrix / Al_8Cu_3Ce interface was observed but appears plausible for prolonged heat treatments. However, this is beyond the scope of this work.

It must be noted that the authors optimized their APM experiments in Figure S1 for mass spectrum resolving power and reduced peak overlap between Ce and Zr. According to the image-hump model, the evaporation fields of Al and Zr are predicted as 19 and 28 V nm^{-1}, respectively [25]. This difference can result in preferential retention or evaporation that may blur the Al-matrix / Al_8Cu_3Ce interface. However, no differences have been found between Al_8Cu_3Ce / Al-matrix and Al-matrix / Al_8Cu_3Ce interfaces with respect to the evaporation sequence. The local composition may be disturbed by thermally activated surface migration. This has been observed by Pogatscher et al. [44] in Si-containing Al alloys as segregation

towards crystallographic poles. Such artefacts have not been observed here for the calibrated acquisition parameters, and only subtle indications of crystallographic poles could be identified.

4.3. Qualitative microstructural model

Figure 10 summarizes the above observations in a qualitative microstructural model. During SLM LPBF fabrication, the Al-matrix and the Al_8Cu_3Ce intermetallic are formed during solidification. Dendritic structures are simplified to circles and these structures are represented schematically in blue and red, respectively. As observed by synchrotron XRD in Figure 2, Al-Cu-Ce and Al-Cu-Ce-Zr alloys exhibit similar phases (Al-matrix and Al_8Cu_3Ce) in the as-fabricated condition. Heat-treating the Al-Cu-Ce alloy results in the phase transformation $Al_8Cu_3Ce \rightarrow Al_8Cu_4Ce$. This is facilitated by uninterrupted solute exchange between the intermetallic and the Al-matrix. Due to the low solubility of Ce in the Al-matrix it is unlikely to participate in the reaction [22]. Al can be rejected into the Al-matrix, or Cu can be accumulated by the intermetallic, whereas both exhibit reasonably large diffusivities in an Al-matrix at 350 °C($D_{Al} \sim 5.5 \times 10^{-16}$ $m^2 s^{-1}$ and $D_{Cu} \sim 2.6 \times 10^{-16}$ $m^2 s^{-1}$) [40]. In Figure 10, Al_8Cu_4Ce is represented in purple and within the Al-matrix. As revealed by synchrotron XRD and APM, the $Al_8Cu_3Ce \rightarrow Al_8Cu_4Ce$ phase transformation is suppressed in the Al-Cu-Ce-Zr alloy. Nanoscale Al_3Zr precipitates are formed in the Al-matrix, which are represented in green. At the MPB these precipitates are smaller than away from MPB [8]. Figure 5,Figure 6, andFigure 7 reveal the affinity of Zr towards the Al-matrix / Al_8Cu_3Ce interface. An enrichment zone is formed which acts as diffusion barrier against solute exchange between the Al-matrix and Al_8Cu_3Ce. Thus, Al_8Cu_3Ce is stabilized against transforming into Al_8Cu_4Ce and results in significantly more sluggish transformation kinetics, even after 96 h at 400°C. Implications for the mechanical properties of this phenomenon are multifaceted. As observed by some of the current authors in a previous study, Zr additions increase the hardness due to the precipitation of nanoscale Al_3Zr [8]. However, intermetallic coarsening and spheroidization may also be circumvented by stabilizing Al_8Cu_3Ce [8,45].

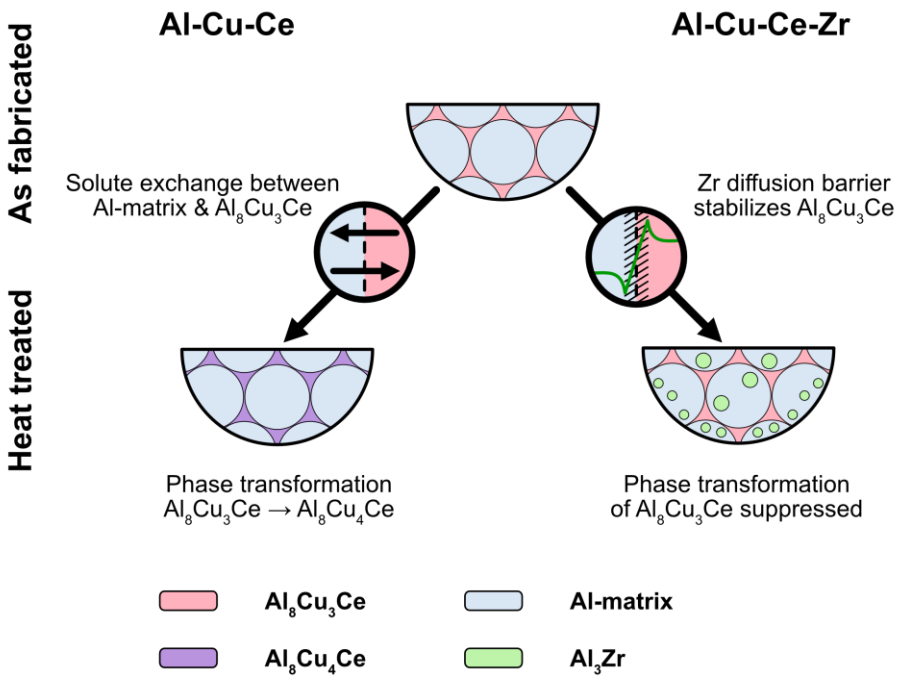

Figure 10 Qualitative microstructural model of the impact of Zr additions to Al-Cu-Ce alloys. During the SLM LPBF processing, both alloys solidify into an Al-matrix and Al_8Cu_3Ce intermetallic. Heat treatment of the Al-Cu-Ce alloy results in the phase transformation $Al_8Cu_3Ce \rightarrow Al_8Cu_4Ce$. In the Al-Cu-Ce-Zr alloy, Zr is enriched on the Al-matrix / Al_8Cu_3Ce interface. This acts as diffusion barrier slowing the $Al_8Cu_3Ce \rightarrow Al_8Cu_4Ce$ kinetics. Nanoscale Al_3Zr are formed within the matrix and provide additional strengthening.

5. Conclusions

The present work reports at the near-atomic scale the mechanism of Zr additions stabilizing the Al_8Cu_3Ce intermetallic in an LPBF manufactured Al-Cu-Ce-Zr alloy. Synchrotron XRD shows that an Al-Cu-Ce alloy without Zr additions exhibits the transformation $Al_8Cu_3Ce \rightarrow Al_8Cu_4Ce$ during subsequent heat treatments. This phase transformation is suppressed in the Al-Cu-Ce-Zr alloy. Calibrated APM reveals quantitative compositions of the Al-matrix, Al_8Cu_3Ce, $(Al,Cu,Si)_4Ce$, Al_2Cu-θ, and Al_3Zr in the as-fabricated and heat-treated conditions, away from and at the MPBs. Zr exhibits an affinity towards the Al-matrix / Al_8Cu_3Ce interface. After the heat treatment, a Zr depletion zone is formed in the Al-matrix, and a Zr enrichment zone is formed at the Al-matrix / Al_8Cu_3Ce interface. The Zr enrichment acts as a

diffusion barrier against solute exchange between Al-matrix and Al_8Cu_3Ce. Thermodynamic modeling underpins that the phase transformation $Al_8Cu_3Ce \rightarrow Al_8Cu_4Ce$ is kinetically suppressed. A qualitative microstructural model summarizes these findings which facilitate the development of LPBF manufactured Al-Cu-Ce-Zr alloys containing the Al_8Cu_3Ce intermetallic with improved high-temperature stability.

Acknowledgements

The authors acknowledge the facilities and scientific assistance of Sydney Microscopy & Microanalysis (SMM) at The University of Sydney, and The University of New South Wales (UNSW). Funding by the AUSMURI program, Department of Industry, Innovation and Science, Australia is acknowledged. This research was co-sponsored by the U.S. Department of Energy, Office of Energy Efficiency and Renewable Energy, Advanced Manufacturing Office, and Vehicle Technologies Office Propulsion Materials Program (YY, KS, and AP). The authors are grateful for the technical assistance and fruitful discussions by Drs Vijay Bhatia (SEM, Sydney), Takanori Sato (APM, Sydney), Sumit Bahl (ORNL) and Sundarsanam Babu (UTK, ORNL). SP is supported by the UNSW Scientia Fellowship scheme.

Conflict of interests

None.

References

[1] S. Manasijevic, R. Radisa, S. Markovic, Z. Acimovic-Pavlovic, K. Raic, Thermal analysis and microscopic characterization of the piston alloy AlSi13Cu4Ni2Mg, Intermetallics. 19 (2011) 486–492. https://doi.org/10.1016/j.intermet.2010.11.011.

[2] W.S. Miller, L. Zhuang, J. Bottema, A.J. Wittebrood, P. De Smet, A. Haszler, A. Vieregge, Recent development in aluminium alloys for the automotive industry, Materials Science and Engineering: A. 280 (2000) 37–49. https://doi.org/10.1016/S0921-5093(99)00653-X.

[3] Y. Wang, L. Zhu, G. Niu, J. Mao, Conductive Al Alloys: The Contradiction between Strength and Electrical Conductivity, Adv. Eng. Mater. 23 (2021) 2001249. https://doi.org/10.1002/adem.202001249.

[4] E.R. Wang, X.D. Hui, G.L. Chen, Eutectic Al–Si–Cu–Fe–Mn alloys with enhanced mechanical properties at room and elevated temperature, Materials & Design. 32 (2011) 4333–4340. https://doi.org/10.1016/j.matdes.2011.04.005.

[5] R.A. Michi, A. Plotkowski, A. Shyam, R.R. Dehoff, S.S. Babu, Towards high-temperature applications of aluminium alloys enabled by additive manufacturing, International Materials Reviews. (2021) 1–48. https://doi.org/10.1080/09506608.2021.1951580.

[6] X.P. Li, X.J. Wang, M. Saunders, A. Suvorova, L.C. Zhang, Y.J. Liu, M.H. Fang, Z.H. Huang, T.B. Sercombe, A selective laser melting and solution heat treatment refined Al–12Si alloy with a controllable ultrafine eutectic microstructure and 25% tensile ductility, Acta Materialia. 95 (2015) 74–82. https://doi.org/10.1016/j.actamat.2015.05.017.

[7] A. Plotkowski, O. Rios, N. Sridharan, Z. Sims, K. Unocic, R.T. Ott, R.R. Dehoff, S.S. Babu, Evaluation of an Al-Ce alloy for laser additive manufacturing, Acta Materialia. 126 (2017) 507–519. https://doi.org/10.1016/j.actamat.2016.12.065.

[8] S. Bahl, K. Sisco, Y. Yang, F. Theska, S. Primig, L.F. Allard, R.A. Michi, C. Fancher, B. Stump, R. Dehoff, A. Shyam, A. Plotkowski, Al-Cu-Ce(-Zr) alloys with an exceptional combination of additive processability and mechanical properties, Additive Manufacturing. 48 (2021) 102404. https://doi.org/10.1016/j.addma.2021.102404.

[9] S. Griffiths, M.D. Rossell, J. Croteau, N.Q. Vo, D.C. Dunand, C. Leinenbach, Effect of laser rescanning on the grain microstructure of a selective laser melted Al-Mg-Zr alloy, Materials Characterization. 143 (2018) 34–42. https://doi.org/10.1016/j.matchar.2018.03.033.

[10] A. Plotkowski, K. Sisco, S. Bahl, A. Shyam, Y. Yang, L. Allard, P. Nandwana, A.M. Rossy, R.R. Dehoff, Microstructure and properties of a high temperature Al–Ce–Mn alloy produced by additive manufacturing, Acta Materialia. 196 (2020) 595–608. https://doi.org/10.1016/j.actamat.2020.07.014.

[11] K. Sisco, A. Plotkowski, Y. Yang, D. Leonard, B. Stump, P. Nandwana, R.R. Dehoff, S.S. Babu, Microstructure and properties of additively manufactured Al–Ce–Mg alloys, Sci Rep. 11 (2021) 6953. https://doi.org/10.1038/s41598-021-86370-4.

[12] A. Hawksworth, W.M. Rainforth, H. Jones, Thermal stability of Al/Al $_{11}$ Ce $_{3}$ and Al/Al $_{11}$ La $_{3}$ /Al $_{3}$ Ni eutectics obtained by Bridgman growth, Materials Science and Technology. 15 (1999) 616–620. https://doi.org/10.1179/026708399101506346.

[13] S. Kou, A criterion for cracking during solidification, Acta Materialia. 88 (2015) 366–374. https://doi.org/10.1016/j.actamat.2015.01.034.

[14] J.L. Murray, A.J. McAlister, The Al-Si (Aluminum-Silicon) system, Bulletin of Alloy Phase Diagrams. 5 (1984) 74–84. https://doi.org/10.1007/BF02868729.

[15] N. Takata, M. Liu, H. Kodaira, A. Suzuki, M. Kobashi, Anomalous strengthening by supersaturated solid solutions of selectively laser melted Al–Si-based alloys, Additive Manufacturing. 33 (2020) 101152. https://doi.org/10.1016/j.addma.2020.101152.

[16] P. Shower, J. Morris, D. Shin, B. Radhakrishnan, J. Poplawsky, A. Shyam, Mechanisms for stabilizing θ′(Al2Cu) precipitates at elevated temperatures investigated with phase field modeling, Materialia. 6 (2019) 100335. https://doi.org/10.1016/j.mtla.2019.100335.

[17] T.B. Massalski, The Al−Cu (Aluminum-Copper) system, Bulletin of Alloy Phase Diagrams. 1 (1980) 27–33. https://doi.org/10.1007/BF02883281.

[18] P. Sepehrband, R. Mahmudi, F. Khomamizadeh, Effect of Zr addition on the aging behavior of A319 aluminum cast alloy, Scripta Materialia. 52 (2005) 253–257. https://doi.org/10.1016/j.scriptamat.2004.10.025.

[19] C.B. Fuller, D.N. Seidman, D.C. Dunand, Mechanical properties of Al(Sc,Zr) alloys at ambient and elevated temperatures, Acta Materialia. 51 (2003) 4803–4814. https://doi.org/10.1016/S1359-6454(03)00320-3.

[20] C. Fuller, J. Murray, D. Seidman, Temporal evolution of the nanostructure of Al(Sc,Zr) alloys: Part I – Chemical compositions of Al(ScZr) precipitates, Acta Materialia. 53 (2005) 5401–5413. https://doi.org/10.1016/j.actamat.2005.08.016.

[21] C. Fuller, D. Seidman, Temporal evolution of the nanostructure of Al(Sc,Zr) alloys: Part II-coarsening of Al(ScZr) precipitates, Acta Materialia. 53 (2005) 5415–5428. https://doi.org/10.1016/j.actamat.2005.08.015.

[22] K.A. Gschneidner, F.W. Calderwood, The Al−Ce (Aluminum-Cerium) system, Bulletin of Alloy Phase Diagrams. 9 (1988) 669–672. https://doi.org/10.1007/BF02883162.

[23] J.D. Poplawsky, B.K. Milligan, L.F. Allard, D. Shin, P. Shower, M.F. Chisholm, A. Shyam, The synergistic role of Mn and Zr/Ti in producing θ′/L12 co-precipitates in Al-Cu alloys, Acta Materialia. 194 (2020) 577–586. https://doi.org/10.1016/j.actamat.2020.05.043.

[24] N. Raghavan, R. Dehoff, S. Pannala, S. Simunovic, M. Kirka, J. Turner, N. Carlson, S.S. Babu, Numerical modeling of heat-transfer and the influence of process parameters on tailoring the grain morphology of IN718 in electron beam additive manufacturing, Acta Materialia. 112 (2016) 303–314. https://doi.org/10.1016/j.actamat.2016.03.063.

[25] B. Gault, M.P. Moody, J.M. Cairney, S.P. Ringer, Atom Probe Microscopy, Springer New York, New York, NY, 2012. https://doi.org/10.1007/978-1-4614-3436-8.

[26] D.J. Larson, T.J. Prosa, R.M. Ulfig, B.P. Geiser, T.F. Kelly, Local Electrode Atom Probe Tomography, Springer New York, New York, NY, 2013. https://doi.org/10.1007/978-1-4614-8721-0.

[27] S. Gražulis, D. Chateigner, R.T. Downs, A.F.T. Yokochi, M. Quirós, L. Lutterotti, E. Manakova, J. Butkus, P. Moeck, A. Le Bail, Crystallography Open Database – an open-access collection of crystal structures, J Appl Crystallogr. 42 (2009) 726–729. https://doi.org/10.1107/S0021889809016690.

[28] M.E. Straumanis, The Precision Determination of Lattice Constants by the Powder and Rotating Crystal Methods and Applications, Journal of Applied Physics. 20 (1949) 726–734. https://doi.org/10.1063/1.1698520.

[29] O.S. Zarechnyuk, P.I. Kripyakevich, I.F. Kolobnev, E.E. Cherkashin, The quaternary compound Ce3 Mn Cu8 Al24 and its crystal structure, Izv. Akad. Nauk SSSR Neorg. Mater. 3 (1967) 182–183.

[30] P. Villars, K. Cenzual, PrCu4Al8 (Cu4PrAl8) Crystal Structure: Datasheet from “PAULING FILE Multinaries Edition – 2012” in SpringerMaterials (https://materials.springer.com/isp/crystallographic/docs/sd_0458767), Springer-Verlag Berlin Heidelberg & Material Phases Data System (MPDS), Switzerland & National Institute for

Materials Science (NIMS), Japan, n.d. https://materials.springer.com/isp/crystallographic/docs/sd_0458767.

[31] J. Schindelin, I. Arganda-Carreras, E. Frise, V. Kaynig, M. Longair, T. Pietzsch, S. Preibisch, C. Rueden, S. Saalfeld, B. Schmid, J.-Y. Tinevez, D.J. White, V. Hartenstein, K. Eliceiri, P. Tomancak, A. Cardona, Fiji: an open-source platform for biological-image analysis, Nat Methods. 9 (2012) 676–682. https://doi.org/10.1038/nmeth.2019.

[32] E. Scheil, Bemerkungen zur Schichtkristallbildung, International Journal of Materials Research. 34 (1942) 70–72. https://doi.org/10.1515/ijmr-1942-340303.

[33] L. Kaufman, H. Bernstein, Computer calculation of phase diagrams With special reference to refractory metals, Academic Press Inc, United States, 1970. http://inis.iaea.org/search/search.aspx?orig_q=RN:02004171.

[34] A.T. Dinsdale, SGTE data for pure elements, Calphad. 15 (1991) 317–425. https://doi.org/10.1016/0364-5916(91)90030-N.

[35] H. Bo, S. Jin, L.G. Zhang, X.M. Chen, H.M. Chen, L.B. Liu, F. Zheng, Z.P. Jin, Thermodynamic assessment of Al–Ce–Cu system, Journal of Alloys and Compounds. 484 (2009) 286–295. https://doi.org/10.1016/j.jallcom.2009.04.083.

[36] C. Zhou, C. Guo, C. Li, Z. Du, Thermodynamic assessment of the phase equilibria and prediction of glass-forming ability of the Al–Cu–Zr system, Journal of Non-Crystalline Solids. 461 (2017) 47–60. https://doi.org/10.1016/j.jnoncrysol.2016.09.031.

[37] B.B. He, Two-dimensional x-ray diffraction, 2018. http://www.vlebooks.com/vleweb/product/openreader?id=none&isbn=9781119356066 (accessed January 24, 2022).

[38] J.R. Croteau, S. Griffiths, M.D. Rossell, C. Leinenbach, C. Kenel, V. Jansen, D.N. Seidman, D.C. Dunand, N.Q. Vo, Microstructure and mechanical properties of Al-Mg-Zr alloys processed by selective laser melting, Acta Materialia. 153 (2018) 35–44. https://doi.org/10.1016/j.actamat.2018.04.053.

[39] F. Czerwinski, Cerium in aluminum alloys, J Mater Sci. 55 (2020) 24–72. https://doi.org/10.1007/s10853-019-03892-z.

[40] K.E. Knipling, D.C. Dunand, D.N. Seidman, Criteria for developing castable, creep-resistant aluminum-based alloys – A review, MEKU. 97 (2006) 246–265. https://doi.org/10.3139/146.101249.

[41] A. Fick, Ueber Diffusion, Ann. Phys. Chem. 170 (1855) 59–86. https://doi.org/10.1002/andp.18551700105.

[42] J. Fiocchi, A. Tuissi, C.A. Biffi, Heat treatment of aluminium alloys produced by laser powder bed fusion: A review, Materials & Design. 204 (2021) 109651. https://doi.org/10.1016/j.matdes.2021.109651.

[43] Y. Li, Z. Liu, J. Zhou, Q. Xia, Microstructure and mechanical properties of Al-Cu-Mg-Ag alloyed with Ce, Transactions of Nonferrous Metals Society of China. (2007) s266–s270.

[44] S. Pogatscher, S.S.A. Gerstl, J.F. Löffler, P.J. Uggowitzer, Atom Probe Tomography Investigations of Modified Early Stage Clustering in Si-Containing Aluminum Alloys, Acta Phys. Pol. A. 128 (2015) 643–647. https://doi.org/10.12693/APhysPolA.128.643.

[45] D.R. Manca, A.Yu. Churyumov, A.V. Pozdniakov, A.S. Prosviryakov, D.K. Ryabov, A.Yu. Krokhin, V.A. Korolev, D.K. Daubarayte, Microstructure and Properties of Novel Heat Resistant Al–Ce–Cu Alloy for Additive Manufacturing, Met. Mater. Int. 25 (2019) 633–640. https://doi.org/10.1007/s12540-018-00211-0.

Supplementary

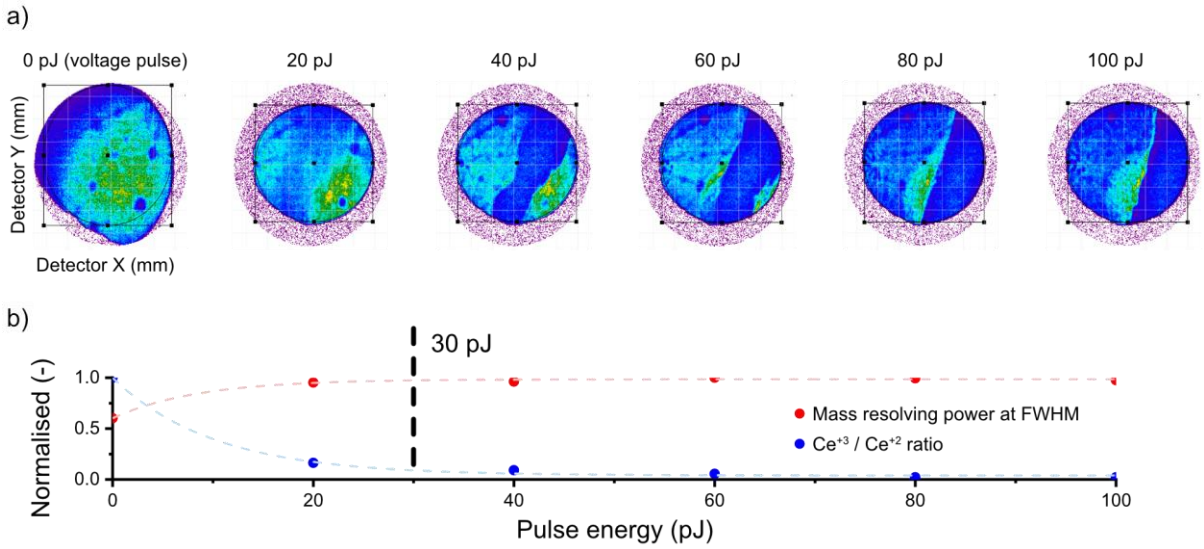

Figure S1 Laser energy calibration before data acquisition. a) Detector event maps for energies ranging from 0 to 100 pJ. b) Normalized plot for the mass resolving power at FWHM and the Ce^{+3}/Ce^{+2} ratio indicate 30 pJ as suitable laser energy.

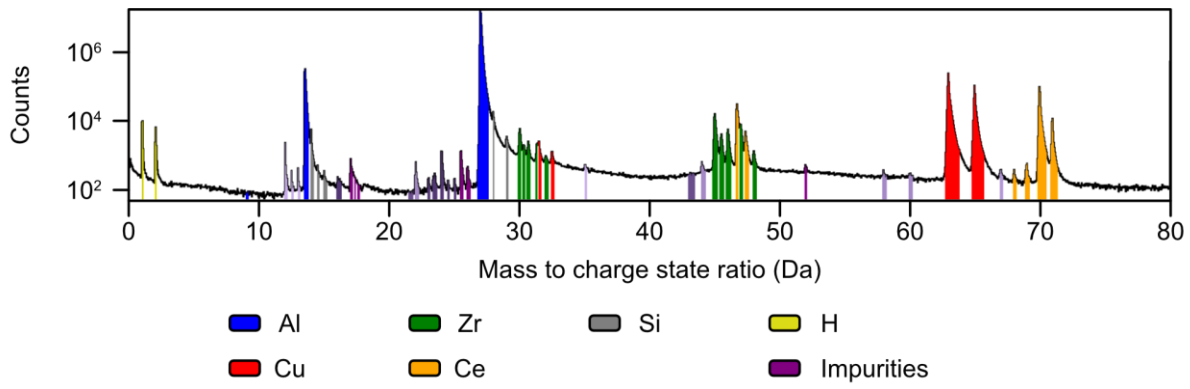

Figure S2 Exemplarily mass spectrum of the Al-Cu-Ce-Zr alloy. H and impurity artefacts are ignored for analyses. Laser pulsing with 30 pJ minimizes the overlap of $^{94}Zr^{+2}$ and $^{140}Ce^{+3}$ at 40-50 Da.